RESEARCH ARTICLE | NOVEMBER 27 2023

On the origin and elimination of cross coupling between tunneling current and excitation in scanning probe experiments that utilize the qPlus sensor

Michael Schelchshorn ; Fabian Stilp ; Marco Weiss ; Franz J. Giessibl

Rev. Sci. Instrum. 94, 113704 (2023)
https://doi.org/10.1063/5.0151615

Review of Scientific Instruments | ARTICLE | pubs.aip.org/aip/rsi

On the origin and elimination of cross coupling between tunneling current and excitation in scanning probe experiments that utilize the qPlus sensor

Cite as: Rev. Sci. Instrum. 94, 113704 (2023); doi: 10.1063/5.0151615
Submitted: 23 March 2023 • Accepted: 26 October 2023 •
Published Online: 27 November 2023

View Online Export Citation CrossMark

Michael Schelchshorn,[a] Fabian Stilp, Marco Weiss, and Franz J. Giessibl[a]

AFFILIATIONS

University of Regensburg, Institute of Experimental and Applied Physics, Universitätsstrasse 31, D-93040 Regensburg, Germany

[a]**Authors to whom correspondence should be addressed:** michael.schelchshorn@ur.de and franz.giessibl@ur.de

ABSTRACT

The qPlus sensor allows for the simultaneous operation of scanning tunneling microscopy (STM) and atomic force microscopy (AFM). When operating a combined qPlus sensor STM/AFM at large tunneling currents, a hitherto unexplained tunneling current-induced cross coupling can occur, which has already been observed decades ago. Here, we study this phenomenon both theoretically and experimentally; its origin is voltage drops on the order of μV that lead to an excitation or a damping of the oscillation, depending on the sign of the current. Ideally, the voltage drops would be phase-shifted by $\pi/2$ with respect to a proper phase angle for driving and would, thus, not be a problem. However, intrinsic RC components in the current wiring lead to a phase shift that does enable drive or damping. Our theoretical model fully describes the experimental findings, and we also propose a way to prevent current-induced excitation or damping.

I. INTRODUCTION

Scanning tunneling microscopy (STM)[1–3] and atomic force microscopy (AFM)[4,5] allow for mapping, identification, and manipulation of individual atoms and molecules on various surfaces and samples.[6–13] While the operation of STM depends on a current flow between the tip and the sample and is thus limited to conductive tips and surfaces, AFM utilizes the forces between atoms of the tip and the surface for image generation.

In addition to the technical challenges of STM, however, AFM faces extra experimental difficulties, e.g., a non-monotonic force–distance behavior, long-range contributions due to van der Waals interactions, and a jump-to-contact phenomenon;[12] atomic resolution with AFM was thus not achieved until 1992,[7,14,15] six years after the method was originally introduced. The benchmark test for atomic resolution, resolving the 7 × 7 reconstruction of the Si(111) surface, had to wait another three years[16] and ultimately became possible by employing frequency modulation AFM (FM-AFM), a method that was introduced four years earlier to resolve micrometer sized magnetization patterns in a fast and sensitive non-contact imaging mode.[17]

Quartz tuning forks as used in wrist watches have been used in scanning probe microscopy for a long time, for instance, in acoustic near-field microscopy,[18] for distance control in scanning near-field optical microscopy,[19] and in cryogenic scanning force microscopy.[20] The qPlus sensor is a stiff quartz cantilever that was originally also built from a quartz tuning fork,[21] with one of the prongs being attached to a heavy substrate, while the other prong was fitted with a probe tip. As atomic resolution was soon obtained after its invention,[22] its popularity grew rapidly and it is now used in hundreds of instruments all over the world.[13]

With its small oscillation amplitudes and possibility to use metallic tips, the qPlus sensor facilitates simultaneous STM and AFM in one instrument. However, when measuring two signals, such as the tunneling current and the signal resulting from the forces at the tip, at the same time, a cross coupling can occur. This effect has been observed since the early years of combined STM/AFM experiments using qPlus sensors; a typical solution is suggested by Heyde *et al.*[23] who mounted the tip using an insulating epoxy onto the qPlus sensor and provided an extra wire that carries the tunneling current or bias voltage. Although this method prevents cross coupling effectively,[24] the mechanic effect of the wire often leads to reduced Q factors and multiple resonances.

Examples of cross coupling between tunneling current and frequency shift and the origin thereof have previously been discussed in the literature: Weymouth *et al.*[25] reported a crosstalk between current and force, leading to a repulsive "phantom" force on samples with limited conductivity, such as semiconductors. This phantom force leads to a reduction in the attractive electrostatic force. Majzik *et al.*[26] analyzed the non-idealities of current-to-voltage converters, such as the STM preamplifier, and virtual ground issues (the oscillation of the virtual ground potential of the STM preamplifier) as a possible reason for a crosstalk between tunneling current and deflection measurement: an unwanted capacitive coupling of the STM virtual ground to the input of the AFM preamplifier changes the deflection signal obtained by the latter; an improved sensor design (similar to Refs. 23 and 27) lowers the coupling between the STM and AFM channels. Replacing the internal coaxial cable with a double-shielded one reduces the stray capacitance further.

In this study, we report on a cross coupling that inflicts a change in the drive amplitude (excitation signal) of the sensor in our setup, depending on the sign of the tunneling current. At one bias polarity, the cross coupling acts as an excitation of the oscillation, whereas in the opposite bias, it appears as a damping. The root cause of this current-induced apparent dissipation is that while the piezoelectric effect is used to generate an electrical current from the vibration, the opposite is also true. A modulation of the voltage at the electrodes on the sensor will induce a deflection. In the same way as microphones can be used as loudspeakers, sensors often can serve as actuators and vice versa. Such a back-action of the deflection detection on the oscillator is often observed, in optical setups as well as in piezoresistive detection.[28]

We find that our qPlus sensor bends by ~180 pm when the differential voltage between the STM electrode and the deflection electrodes (see Fig. 2) changes by 1 V (see Sec. V A). Thus, an AC voltage at the sensor's resonance frequency applied to that tip electrode merely needs an amplitude of 1 μV to excite the sensor to an amplitude of about 36 pm if the quality factor of the sensor is $Q = 200\,000$; in fact, that exact electrode can intentionally be used to excite the oscillation. If the tunneling current that flows through one of the sensor electrodes modulates its electrical potential by 1 μV at a phase of 90° (at resonance), a change in the excitation signal of ±72% will occur for an amplitude setpoint of 50 pm. In theory, the tunneling current has a phase shift of 180° with respect to the sensor deflection and, therefore, should not alter the excitation signal. In practice, cable resistance and parasitic or intentional capacities introduce RC circuits into the current line that cause an additional phase shift, resulting in unwanted damping or excitation.

We present a model that explains the cross coupling between tunneling current and sensor excitation, supported by experiments and supplemented by verified measures on how to prevent or at least minimize crosstalk.

II. GENERAL CONCEPTS

A. STM

Scanning tunneling microscopy (STM) is based on the detection of a tunneling current between a sharp, metallic probe tip and a conductive sample, of which the surface is scanned at a distance of a few 100 pm. If a bias voltage V_B is applied between the tip and the sample, a quantum-mechanical tunneling current flows,[6] which depends exponentially on the distance z between the tip apex and the sample surface,[2]

$$I_t(z) = I_0 \times \exp(-2\kappa z), \tag{1}$$

where $I_0 = I_t(z = 0)$ is determined by the bias and κ is the decay constant, which depends on the work functions of the tip and the sample.

B. FM-AFM

In frequency modulation atomic force microscopy (FM-AFM), the quartz cantilever is driven at resonance while fixing the oscillation amplitude A by feeding the 90° phase-shifted deflection signal through a Proportional–Integral (PI) amplitude controller back to the cantilever. When the oscillating tip is subject to a nonzero tip–sample force gradient k_{ts}, the oscillation frequency changes from the fundamental eigenfrequency of the free cantilever f_0 by the frequency shift Δf,[29] which is given by $f_0 \times \langle k_{ts}(z_0)\rangle/(2k)$, where the pointed brackets indicate an averaging process explained in Ref. 12.

Another experimental observable of FM-AFM with oscillating cantilevers, such as qPlus, is the dissipative component of the tip–sample interaction.[30] The studies of dissipation and atomic manipulation offer a fundamental approach to the investigation of molecules and single chemical bonds as well as friction;[31,32] dissipation data are explained using the Tomlinson–Prandtl model[33–36] of friction as a plucking action on single atoms.

The energy dissipated over one oscillation cycle ΔE_{ts} is given by[36]

$$\Delta E_{ts} = \oint \vec{F}_{ts}\, d\vec{z} = -\int_0^{2\pi} F_{ts}(z + A\cos\phi) A \sin\phi\, d\phi, \tag{2}$$

which is nonzero if a hysteresis occurs in the tip–sample force curve $F_{ts}(z)$ over the z-range covered by the oscillating cantilever. In order to keep the amplitude A constant, the drive signal X'_{drive} changes as follows:[12]

$$\frac{X'_{drive}}{X_{drive}} = 1 + \frac{Q}{2\pi}\frac{\Delta E_{ts}}{E}, \tag{3}$$

where X_{drive} is the amplitude of the excitation signal of the free oscillation (with a frequency $f = f_0$ and a phase shift $\phi_{drive} = 90°$ with respect to the sensor oscillation); internal dissipation in the (free) motion of the cantilever itself is defined by its quality factor Q, and the total oscillation energy for a cantilever with stiffness k and oscillation amplitude A is given by $E = \frac{1}{2} k A^2$.

C. Dynamic STM

When combining AFM and STM measurements by FM-AFM, the electronic tunneling current between the tip and the sample varies with time due to the sensor's oscillation. Assuming a harmonic tip motion with amplitude A and angular frequency $\omega = 2\pi \times f = \sqrt{(k + k_{ts}(z_0))/m^*}$, without higher harmonics, the instantaneous tip–sample separation can be written as

$$z(t) = z_0 + A \times \cos(\omega t), \tag{4}$$

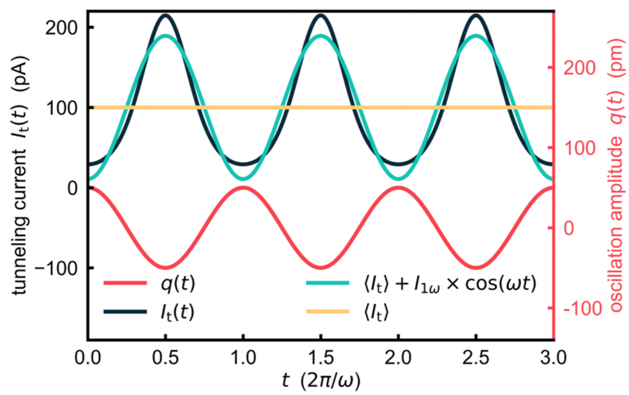

FIG. 1. The tunneling current $I_t(t)$ as a function of time computed according to Eq. (5), the time-averaged current $\langle I_t \rangle$, and the Fourier series [Eq. (6)] up to first order in ω. The oscillation amplitude $q(t) = A \times \cos(\omega t)$ is plotted for reference. The parameters used for the plots are $A = 50$ pm, $\kappa = 1 \times 10^{10}$ m^{-1}, and $\langle I_t \rangle = 100$ pA.

where z_0 is the tip–sample distance at rest, which is modulated by the cantilever motion $q(t) = A \times \cos(\omega t)$. In accordance with Eq. (1), we obtain the tunneling current as a function of time t (see Fig. 1),

$$I_t(t) = I_{z_0} \times \exp\left(-2\kappa A \times \cos(\omega t)\right) \tag{5}$$

with $I_{z_0} = I_0 \times \exp(-2\kappa z_0)$. As $I_t(t)$ is periodic in time, it can be expanded in a Fourier series,

$$I_t(t) = \langle I_t \rangle + I_{1\omega} \times \cos(\omega t) + I_{2\omega} \times \cos(2\omega t) + \cdots, \tag{6}$$

where the second order term $I_{2\omega} \times \cos(2\omega t)$ and all higher-order terms are small compared to the first order term if the oscillation amplitude A is small compared to the inverse decay rate of the tunneling current $1/\kappa$. The DC and first order terms are given by[37]

$$\langle I_t \rangle = I_{z_0} \Im_0(2\kappa A) \quad \text{and} \quad I_{1\omega} = -2\langle I_t \rangle \frac{\Im_1(2\kappa A)}{\Im_0(2\kappa A)}, \tag{7}$$

respectively, where $\Im_n$ is the modified Bessel function of first kind of order n. $\langle I_t \rangle$ is equal to the time-average of $I_t(t)$ over one oscillation period; it denotes the measured value of the tunneling current in experiment as the bandwidth of the tunneling current amplifier is typically small compared to the oscillation frequency.[38] When using a tunneling current amplifier with a high bandwidth, the first order term can be used to measure the decay rate and thus the work function at atomic resolution.[39]

III. EXPERIMENTAL SETUP AND FIRST OBSERVATION OF APPARENT DISSIPATION

A. Experimental setup

All measurements shown here have been conducted using a home-built low-temperature ($T \approx 5.5$ K) combined scanning tunneling and atomic force microscope operating in ultra-high vacuum ($p \approx 5 \times 10^{-11}$ mbar).[40,41]

The sensor used for combined STM- and AFM-measurements in our microscope is based on a third-generation qPlus sensor (Type S1.0 in Table 1 in Ref. 13) with a stiffness of $k = 1800$ N/m. An etched tungsten tip is attached to its oscillating prong, and an electrode dedicated to collecting the tunneling current is applied on one side of the oscillating quartz beam as shown in Fig. 2. Additional electrodes are located on each side of the beam, whereby electrodes on opposite sides are electrically connected. The two corresponding AFM contacts on the sensor serve as a differential input for the AFM preamplifier. Our sensor is driven by connecting the amplitude drive signal to the z-terminal of the xyz scan piezo to shake the sensor holder. The amplitude of this AC voltage serves as the excitation signal X'_{drive} in the measurement: a positive amplitude corresponds to a driving, while a negative value corresponds to a damping.

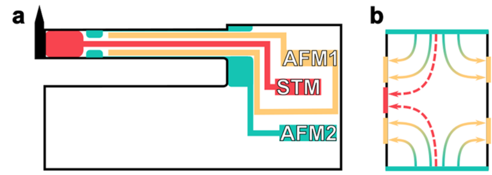

FIG. 2. Geometry of the qPlus sensor in our microscope. (a) Electrode layout. Two AFM contacts are used for differential deflection measurement and one STM contact for detecting the tunneling current. (b) Cross section through the oscillating beam in (a). The electric field distribution caused by a deflection of the sensor (solid arrows) is shown. This phenomenon is known as the piezoelectric effect, of which the inverse is also possible: a modulation of the potential V_s on the STM electrode leads to a deflection of around 180 pm/V.

The resonance frequency f_0 and quality factor Q are obtained from a frequency sweep: here, $f_0 = 20\,419.3$ Hz and $Q = 210\,320$ for measurements with bias applied to the tip and $f_0 = 20\,383.6$ Hz and $Q = 112\,781$ for measurements with bias applied to the sample.

The origin of cross coupling, between the excitation signal and the tunneling current, is directly related to the electrode layout on the qPlus sensor discussed above and the electrical connections to tip and sample. Figure 3 schematically shows our sensor and sample with connections to the bias output and the STM preamplifier, respectively. Two distinct bias configurations are possible: bias applied at the tip (A1–A2/B1–B2) and bias applied at the sample (A1–B1/A2–B2).

The line between the bias voltage output and the microscope head includes an external resistor $R_B = 110$ kΩ and a coaxial cable leading to the microscope, which has a negligible resistance. Inside the microscope, high-resistance coaxial cables are used to prevent thermal coupling with the outside: the resistance R_w of such a cable is ~50 Ω.[41] The combined capacitance C of the coaxial cables to ground (which is typically around 100 pF/m) represents the capacitance between $V_s(t)$ and ground potential since the capacitance of the tip–sample junction is on the order of a few picofarads and thus small enough to be neglected. Using a multimeter, $C = (780 \pm 20)$ pF and $C_w = (390 \pm 10)$ pF were measured.

The resistance $R = R_B + R_w$ and capacitance C produce a passive low-pass filter to reduce the high-frequency noise in the bias voltage signal V_B. The transfer function of this RC element is given by

$$\frac{V_{\text{out}}}{V_{\text{in}}} = \frac{\frac{1}{i\omega C}}{R + \frac{1}{i\omega C}} = \frac{1}{1 + i\omega RC}, \tag{8}$$

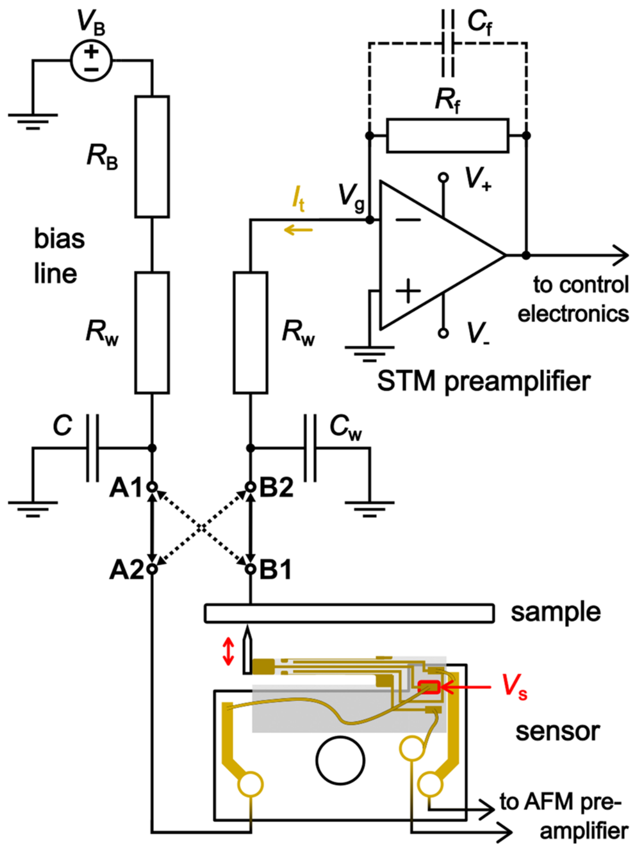

FIG. 3. Relevant section of the microscope's STM electronics. With the inverting input of the STM preamplifier connected accordingly, the bias is applied either at the tip (A1–A2/B1–B2) or at the sample (A1–B1/A2–B2). The common reference potential is the ground of the microscope chamber. The positive direction of the tunneling current (technical current direction) is indicated by an arrow; the measured tunneling current and the bias voltage have an opposite sign.

where the time constant $\tau = RC$ is inverse to an angular cutoff frequency $\omega_c = 1/\tau$; the output is phase-shifted with respect to the input by $-\arctan(\omega RC)$. For frequencies $f \ll f_c = \omega_c/(2\pi) = 1.9$ kHz, the output is essentially equal to the input. For $f = f_c$, the amplitude of V_{out} is reduced to $V_{in}/\sqrt{2}$ with a phase shift of $-\pi/4$. For even higher frequencies, the amplitude of V_{out} is reduced further and the phase shift saturates at $-\pi/2$.

The other connection from the microscope head leads to the inverting input of the STM preamplifier, which is located just outside the vacuum chamber, via another high-resistance coaxial cable. The STM preamplifier is based on a type AD8616[42] with a supply voltage of $V_\pm = \pm 3$ V, wired as a transimpedance amplifier (see Fig. 3), with a feedback resistor $R_f = 100$ MΩ and a parasitic capacitance $C_f = 0.69$ pF.[38] The latter prevents the amplifier from going into positive feedback: the RC element formed by R_f and the large input capacitance of the STM preamplifier (dominated by C_w), combined with the amplifier's internal phase shift of $-\pi/2$, would otherwise increase the total phase shift of the feedback loop to $-\pi$ at a frequency where the loop gain is still greater than unity.[43,44] By adding C_f, the phase shift reverts back to $-\pi/2$, crossing $-3\pi/4$ at a frequency $f_z = 1/(2\pi R_f C_f) = 2.3$ kHz.

With a periodic input, such as the tunneling current, Eq. (5), the phase shift of the feedback loop causes the virtual ground V_g to oscillate. This effect was characterized by Junk,[45] who analyzed the modulation of V_g and its link to cross coupling by considering the influence on the electrostatic interaction between tip and sample. It was concluded that the electrostatic force resulting from virtual ground fluctuations can only induce a tiny fraction of the observed apparent dissipation, prompting the present study.

1. Bias at tip

Virtual ground issues (as discussed also in Ref. 26) motivate a bias configuration, where V_g is not connected to the tip but rather the sample (A1–A2/B1–B2 in Fig. 3); here, it is experimentally found that the change in the excitation signal as a function of the tunneling current is the same if the STM preamplifier is disconnected and its port at the microscope grounded compared to the case with the STM preamplifier connected, leading to the same apparent dissipated energy in both cases [see Appendix A 1 with Fig. 11(a)]. Thus, if the bias is applied to the tip, any oscillation of the virtual ground V_g or phase shift in our circuit resulting from non-idealities of our STM preamplifier can be neglected ($V_g = 0$ V).

The origin of apparent dissipation observed in this case is linked to the combined effect of an oscillating junction resistance and a high impedance of the bias voltage supply. The RC element in the bias line leads to an oscillating potential $V_s(t)$ at the STM electrode of the qPlus sensor, which is phase-shifted with respect to the tip oscillation. Due to the piezoelectric nature of the qPlus sensor, this tunneling current-induced modulation of $V_s(t)$ can couple to the cantilever deflection, thereby leading to an apparent dissipation in measurement.

Data for different resistors R_B verify that the apparent dissipated energy goes to zero when the RC element is eliminated by removing R_B [see Appendix A 2 with Table II as well as Sec. V B with Fig. 9(a)].

2. Bias at sample

Fluctuations of the virtual ground cannot be neglected, when the bias is applied to the sample (A1–B1/A2–B2 in Fig. 3). While in this case, the effect of the RC low-pass in the bias line on the apparent dissipation is negligible (see Appendix A 2 with Table II), the origin of cross coupling is directly related to the oscillation of the virtual ground of the STM preamplifier, which is phase-shifted with respect to the tunneling current. Fluctuations of V_g induce a modulation of $V_s(t)$ at the STM electrode of the qPlus sensor and again provoke an apparent dissipation via the inverse piezoelectric effect.

Data taken with and without the STM preamplifier verify that, for bias applied to the sample, the apparent dissipation goes to zero as V_g goes to 0 V [see Appendix A 2 and Sec. V B with Fig. 9(b)].

B. Measurement of apparent dissipation

Equation (3) for the dissipated energy over one oscillation cycle needs to be modified if crosstalk between the tunneling current and excitation occurs, replacing ΔE_{ts} by an apparent dissipation $\Delta E_{ts}^{apparent}$ with

$$\Delta E_{ts}^{apparent} = \Delta E_{ts} + \Delta E_{crosstalk} \tag{9}$$

or

$$\Delta E_{\mathrm{ts}}^{\mathrm{apparent}} = 2\pi \frac{E}{Q}\left(\frac{X'_{\mathrm{drive}}}{X_{\mathrm{drive}}} - 1\right). \tag{10}$$

The experimental manifestation of a change in the driving signal from X_{drive} (freely oscillating cantilever) to X'_{drive} (cantilever that oscillates close to the sample) only allows us to determine a combined effect of ΔE_{ts} and $\Delta E_{\mathrm{crosstalk}}$ as noted in Eq. (9). While self-excitation from tip–sample interaction (negative ΔE_{ts}), for instance by stochastic motion of hydrogen molecules on Cu(111),[46] has been reported, we can expect (on our bare sample) ΔE_{ts} to be very small such that the crosstalk term is directly represented by the apparent dissipation signal; $\Delta E_{\mathrm{crosstalk}} \approx \Delta E_{\mathrm{ts}}^{\mathrm{apparent}}$ can be positive or negative.

To study the apparent dissipation, z-spectroscopy measurements were performed over a flat Cu(111) surface: the tip was approached toward the sample in STM feedback beforehand, then retracted 500 pm from the surface, decreasing the magnitude of the tunneling current $|\langle I_{\mathrm{t}}\rangle|$ (forward "ramping" direction), and approached back to the starting point, increasing $|\langle I_{\mathrm{t}}\rangle|$ again (backward "ramping" direction). Due to piezo-creep during measurement, the tunneling current at the end can differ from the value at the beginning (see Appendix A 2).

Experiments with $R_{\mathrm{B}} = 110\ \mathrm{k\Omega}$ were performed for tip biases $V_{\mathrm{B}} = \pm 0.5$ mV, $V_{\mathrm{B}} = \pm 1.0$ mV, and $V_{\mathrm{B}} = \pm 10$ mV for 16 different amplitude setpoints between $A = 10$ pm and $A = 400$ pm. Additional measurements with a different resistor ($R_{\mathrm{B}} = 10\ \mathrm{k\Omega}$) and no external resistor ($R_{\mathrm{B}} = 0\ \Omega$) were carried out with a tip bias $V_{\mathrm{B}} = \pm 1.0$ mV for amplitudes between $A = 10$ pm and $A = 100$ pm.

For sample biases $V_{\mathrm{B}} = \pm 1.0$ mV and $V_{\mathrm{B}} = \pm 10$ mV, measurements with $R_{\mathrm{B}} = 110\ \mathrm{k\Omega}$ and, additionally, $R_{\mathrm{B}} = 0\ \Omega$ were carried out for six amplitude setpoints between 10 and 100 pm.

All additional measurements (for $R_{\mathrm{B}} = 10\ \mathrm{k\Omega}$ and $R_{\mathrm{B}} = 0\ \Omega$) are discussed in Sec. V B.

In Fig. 4, the apparent dissipated energy $\Delta E_{\mathrm{ts}}^{\mathrm{apparent}}$ [Eq. (10)] for $R_{\mathrm{B}} = 110\ \mathrm{k\Omega}$ is plotted vs the tunneling current $\langle I_{\mathrm{t}}\rangle$ for three different amplitudes A from the data of excitation X'_{drive} from z-spectroscopy measurements for different bias voltages applied to the tip [Fig. 4(a)] and the sample [Fig. 4(b)]. The backward direction generally yields the same results as the forward direction (see Appendix A 2 with Fig. 12).

From the graphs (Fig. 4), the apparent dissipation indicates the following three substantial characteristics:

1. $\Delta E_{\mathrm{ts}}^{\mathrm{apparent}}$ is linear as a function of the tunneling current $\langle I_{\mathrm{t}}\rangle$. The maximum range of the tunneling current is influenced by the chosen voltage bias V_{B} and the tip–sample distance. The linearity breaks down for $A \geq 100$ pA for small bias voltages V_{B}; when focusing on small currents, $\langle I_{\mathrm{t}}\rangle < 1$ nA, the linear relation holds to a good approximation.
2. $\Delta E_{\mathrm{ts}}^{\mathrm{apparent}}$ has the opposite (the same) sign compared to the tunneling current $\langle I_{\mathrm{t}}\rangle$ if the bias is applied to the tip (sample); for $\langle I_{\mathrm{t}}\rangle < 0$ A, the oscillation of the tip appears damped (driven), while for $\langle I_{\mathrm{t}}\rangle > 0$ A, the oscillation appears driven (damped). At a constant current, $\Delta E_{\mathrm{ts}}^{\mathrm{apparent}}$ is independent of the magnitude of V_{B} (again considering only small currents).
3. $\Delta E_{\mathrm{ts}}^{\mathrm{apparent}}$ depends on the amplitude A. Larger amplitudes generally provoke a larger apparent dissipation.

In summary, for a given amplitude A, the apparent dissipation depends only on the tunneling current $\langle I_{\mathrm{t}}\rangle$, whereby the sign of $\langle I_{\mathrm{t}}\rangle$ determines if the apparent dissipation is positive or negative.

The values for the apparent dissipated energy per oscillation cycle per tunneling current $\Delta E_{\mathrm{ts}}^{\mathrm{apparent}} / \langle I_{\mathrm{t}}\rangle$ from a linear fit for the

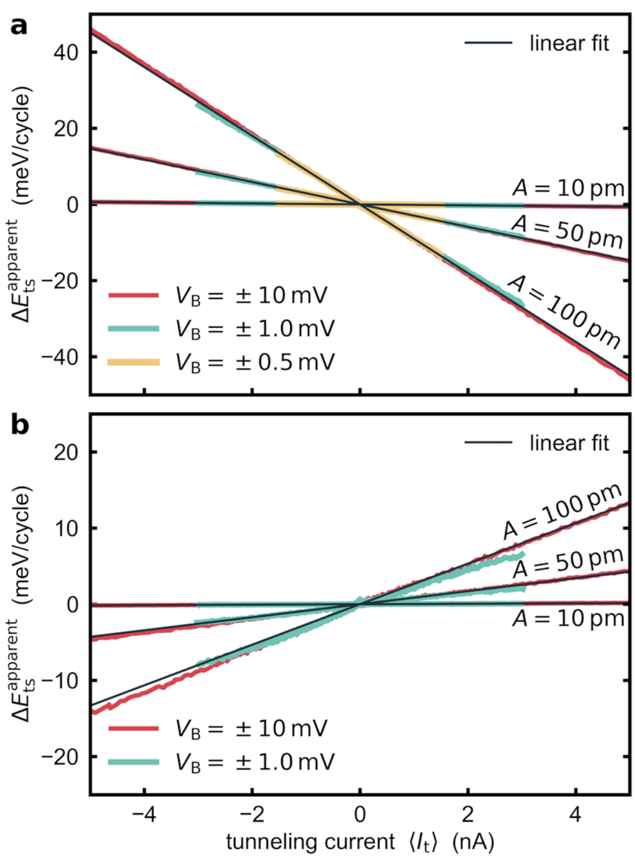

FIG. 4. Apparent dissipation per oscillation cycle $\Delta E_{\mathrm{ts}}^{\mathrm{apparent}}$ vs tunneling current $\langle I_{\mathrm{t}}\rangle$ at different bias voltages and three different amplitudes A. (a) Bias applied to the tip. (b) Bias applied to the sample. All curves intersect at $\langle I_{\mathrm{t}}\rangle = 0$ nA and $\Delta E_{\mathrm{ts}}^{\mathrm{apparent}} = 0$ meV. A linear fit for each of the three amplitudes in both cases yields the values listed in Table I.

TABLE I. Values for the apparent dissipated energy per oscillation cycle per tunneling current $\Delta E_{\mathrm{ts}}^{\mathrm{apparent}} / \langle I_{\mathrm{t}}\rangle$ for three different amplitudes A and two distinct bias configurations, obtained from curves in Fig. 4 by a linear fit.

	$\Delta E_{\mathrm{ts}}^{\mathrm{apparent}}/\langle I_{\mathrm{t}}\rangle$ (meV/cycle/nA)	
Amplitude A (pm)	Bias at tip	Bias at sample
10	−0.13	0.03
50	−2.95	0.86
100	−9.02	2.66

three amplitudes shown in Fig. 4 are given in Table I. The magnitude of the apparent dissipation is generally smaller by ~70% if the bias is applied to the sample, instead of the tip.

IV. HARMONIC MODEL TO EXPLAIN APPARENT DISSIPATION

A. Oscillation of the sensor potential

The (periodic) sensor potential $V_s(t)$ can be written as

$$V_s(t) = V_{s,0} + V_{s,1} \times \cos(\omega t + \phi_{s,1}) + V_{s,2} \times \cos(2\omega t + \phi_{s,2}) + \cdots. \tag{11}$$

For the two bias configurations in Sec. III A, different ways of determining the first order modulation of the sensor potential $V_{s,1} \times \cos(\omega t + \phi_{s,1})$ are presented.

1. Bias at tip

For the calculation of the potential $V_s(t)$ applied at the STM electrode of our sensor, a simplification of the circuit in Fig. 3 is considered. The resistance R in the bias line and the capacitance C between the STM electrode and the chamber ground act as a passive RC element. The tip–sample capacitance is much smaller than the cable capacitance and can be neglected such that the tip–sample junction can be represented simply by an oscillating resistance $R_J(t)$. As no dependence of the apparent dissipation on V_g was found (see Appendix A 1) and the impedance of the wire is small compared to R and $R_J(t)$, V_g can be set to 0 V and directly connected at the sample. The simplified circuit is shown in Fig. 5(a).

Kirchhoff's current law for this circuit yields an inhomogeneous linear differential equation for $V_s(t)$,

$$\frac{V_B - V_s(t)}{R} = C\,\frac{\mathrm{d}V_s(t)}{\mathrm{d}t} + \frac{V_s(t)}{R_J(t)} \tag{12}$$

or, assuming $V_s(t)/R_J(t) = -I_t(t)$ with $I_t(t)$ as described in Sec. II C,

$$\frac{\mathrm{d}V_s(t)}{\mathrm{d}t} = -\frac{1}{RC}\,V_s(t) + \left(\frac{I_t(t)}{C} + \frac{V_B}{RC}\right). \tag{13}$$

The solution of Eq. (13) [for $I_t(t)$ given by Eq. (5)] is presented in Appendix B 2. The first order solution [assuming $I_t(t) = \langle I_t\rangle + I_{1\omega}\cos(\omega t)$] in the steady state is given by (see Appendix B 1)

$$V_s(t) = V_B + R\,\langle I_t\rangle + \frac{R\,I_{1\omega}\,\cos(\omega t - \arctan(\omega RC))}{\sqrt{1+(\omega RC)^2}}. \tag{14}$$

Given a sinusoidal current, $V_s(t)$ is thus also harmonic with the constant offset $V_{s,0} = V_B + R\langle I_t\rangle$ plus a cosine with amplitude $V_{s,1} = R\,I_{1\omega}/\sqrt{1+(\omega RC)^2}$, phase-shifted with respect to the sensor oscillation by

$$\phi_{s,1} = -\arctan(\omega RC). \tag{15}$$

In our microscope setup, we have $\omega/(2\pi) \approx 20.4$ kHz and $C = 780$ pF, so $\phi_{s,1} \approx -85°$ for $R = 110.1$ kΩ.

Both $\phi_{s,1}$ and $V_{s,1}$ depend on the value of $R = R_B + R_w$, as illustrated in Fig. 6(a). As $V_{s,1} \propto R$, removing R_B results not only in a

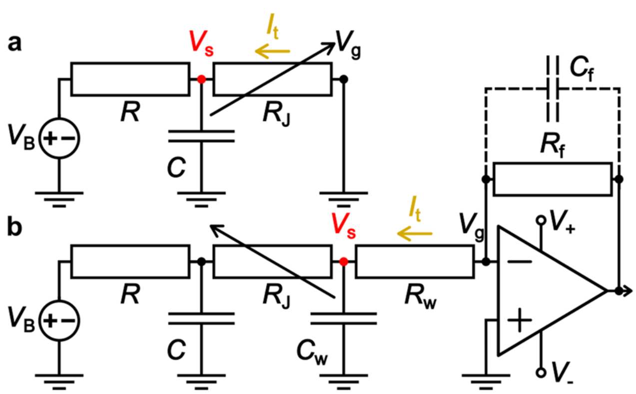

FIG. 5. Simplified form of the circuit from Fig. 3 for the calculation of $V_s(t)$. (a) If the bias is applied to the tip, V_g can be assumed to be at ground. R_w and C_w can be neglected. (b) If the bias is applied to the sample, the virtual ground fluctuations cannot be neglected; the low-pass behavior of the STM preamplifier and its feedback loop has to be considered. The voltages V_B and $V_s(t)$ are measured against common ground (chamber ground of the microscope).

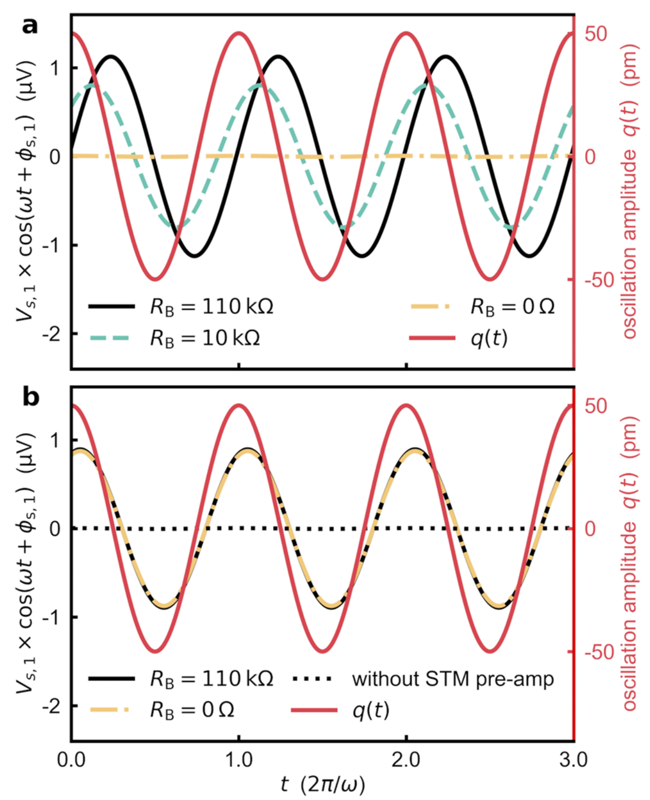

FIG. 6. The AC component of $V_s(t)$ for different values of R_B and $V_B = 1.0$ mV. (a) Bias applied to the tip, $\langle I_t\rangle = -100$ pA. (b) Bias applied to the sample, $\langle I_t\rangle = +100$ pA. The oscillation amplitude of the tip is plotted for comparison. Here, the parameters used are $A = 50$ pm, $\kappa = 1 \times 10^{10}$ m^{-1}, $C = 780$ pF, and $\omega/(2\pi) = 20.4$ kHz. For an opposite sign of the tunneling current, $V_{s,1}$ gains an additional minus sign, which corresponds to mirroring at the x axis. If the sensor bends by 180 pm/V and $Q = 200\,000$, an amplitude of $V_{s,1} = 1\,\mu$V at $\phi_{s,1} = \mp 90°$ will lead to a change in the excitation signal of ±72% at an amplitude setpoint of $A = 50$ pm.

significantly smaller phase shift [Eq. (15)] with respect to the oscillation $q(t)$ of the sensor but also in an equivalently reduced amplitude. Furthermore, $V_{s,1}$ depends linearly on the tunneling current as $I_{1\omega} \propto -\langle I_t \rangle$.

For a negative tunneling current $\langle I_t \rangle$, $V_s(t)$ lags behind the tip oscillation [see Fig. 6(a)] and the phase shift is $\phi_{s,1}$.

For a positive tunneling current $\langle I_t \rangle$, the sign of the bias voltage V_B is reversed; $V_s(t)$ gains an additional minus sign and is, therefore, ahead of the tip oscillation. The additional minus sign can also be interpreted as an additional phase shift of 180°: the phase shift of $V_s(t)$ with respect to the oscillation amplitude $q(t) = A \times \cos(\omega t)$ is then given by $\phi_{s,1} + 180°$.

With $\phi_{s,1} = -85°$, as estimated before in the case of $R = 110.1$ kΩ, we see that for both positive and negative signs of $\langle I_t \rangle$, the phase shift is close to +90° and −90°, respectively; $V_s(t)$ can thus strongly couple to the sensor oscillation as discussed in Sec. IV B.

2. Bias at sample

For the circuit in Fig. 5(b), an analytical solution to $V_s(t)$ does not exist; instead, an LTSpice[47] based simulation is used to determine $V_s(t)$, assuming $I_t(t) \times R_J(t) = \langle I_t \rangle \times [V_B / \langle I_t \rangle - R - R_w]$ with $I_t(t)$ as described in Sec. II C. The AD8616 SPICE Macro Model for the op-amp in Fig. 5(b) is provided by Analog Devices, Inc.;[48] the first order of $V_s(t)$ is extracted using a Fourier decomposition.

Compared to the bias at the tip [Fig. 6(a)], $V_s(t)$ has a positive sign for a positive tunneling current [Fig. 6(b)]. While for $R_B = 110$ kΩ, the absolute value of the amplitude $|V_{s,1}|$ is reduced by around 20%, the phase is significantly smaller: $\phi_{s,1} \approx -19°$. Therefore, $\left| \left(V_{s,1}^{(\text{sample})} \sin(\phi_{s,1}^{(\text{sample})}) \right) \Big/ \left(V_{s,1}^{(\text{tip})} \sin(\phi_{s,1}^{(\text{tip})}) \right) \right| \approx 0.8 \times \sin(\phi_{s,1}^{(\text{sample})}) \Big/ \sin(\phi_{s,1}^{(\text{tip})}) \approx 0.3$, which explains why $\Delta E_{ts}^{\text{apparent}} / \langle I_t \rangle$ (in Sec. III B with Table I) is reduced by 70% if the bias is applied to the sample, compared to the tip [see also the result of Eq. (28)]. Nevertheless, $V_{s,1} \times \cos(\omega t + \phi_{s,1})$ is considerable in both cases; the resulting cross coupling to the excitation is explored in the following.

B. Harmonic oscillator model for the tip's motion

To study the influence of a piezoelectric force on the qPlus sensor motion, $q(t) = A \times \cos(\omega t)$, we consider a one-dimensional harmonic oscillator model. The equation of motion for the sensor tip with an effective mass m^* and stiffness k is

$$m^* \ddot{q}(t) + \frac{m^* \omega_0}{Q} \dot{q}(t) + k\, q(t) = F_{ts}(t) + F_{\text{drive}}(t) + F_{\text{piezo}}(t), \quad (16)$$

where Q is the quality factor and $\omega_0 = 2\pi \times f_0 = \sqrt{k/m^*}$ is the angular resonance frequency of the free cantilever. External forces acting on the cantilever are written on the right-hand side of Eq. (16): (1) $F_{ts}(t)$, the tip–sample force; (2) $F_{\text{drive}}(t) = F_{\text{drive}}^0 \times \cos(\omega t + \phi_{\text{drive}})$, the force of mechanical excitation of the sensor in the FM-AFM mode; and (3) $F_{\text{piezo}}(t) = F_{\text{piezo}}^0 \times \cos(\omega t + \phi_{\text{piezo}})$, the piezoelectric force resulting from the modulation of the sensor voltage $V_s(t)$, which can interfere with the tip's motion, thereby producing an apparent dissipation.

The phases ϕ_{drive} and ϕ_{piezo} are defined in reference to the sensor oscillation $q(t)$. Since a voltage applied to the STM electrode results in an instantaneous force that deflects the sensor by the piezoelectric effect, we set $F_{\text{piezo}}(t) \propto V_{s,1} \times \cos(\omega t + \phi_{s,1})$, and hence, $\phi_{\text{piezo}} = \phi_{s,1}$.

All parameters on the left-hand side of Eq. (16) are well defined (see Sec. III A). Both $F_{\text{drive}}(t)$ and $F_{\text{piezo}}(t)$ are assumed to be harmonic, more specifically, sinusoidal, with the same angular frequency ω as the oscillation $q(t)$. For small deflections from the resting position z_0 or, equivalently, for small amplitudes of $q(t)$, one can assume a parabolic tip–sample interaction potential V_{ts}; then, the force gradient $\left(-\frac{dF_{ts}}{dz}\right)\Big|_{z_0} = \left(\frac{d^2 V_{ts}}{dz^2}\right)\Big|_{z_0}$ is constant over one oscillation cycle and $F_{ts}(t)$ is a linear function of the tip–sample distance $q(t)$ and thus also an harmonic function of time t,

$$F_{ts}(t) = -k_{ts}(z_0) \times q(t) + \textit{const.}, \quad (17)$$

where *const.* = 0 because a zero force would result in a zero deflection $q(t)$. Bringing $F_{ts}(t)$ to the left-hand side of Eq. (16), dividing the whole equation by m^* and using

$$\omega^2 = \frac{k + k_{ts}}{m^*}, \quad (18)$$

one ends up with the differential equation

$$\ddot{q}(t) + \frac{\omega_0}{Q} \dot{q}(t) + \omega^2 q(t) = \frac{F_{\text{drive}}^0}{m^*} \times \cos(\omega t + \phi_{\text{drive}}) + \frac{F_{\text{piezo}}^0}{m^*} \times \cos(\omega t + \phi_{s,1}). \quad (19)$$

Inserting $q(t) = A \times \cos(\omega t)$, carrying out the derivatives, and using a trigonometric identity for the cosine functions on the right-hand side, we have

$$\begin{aligned} \frac{-\omega\omega_0}{Q} A \times \sin(\omega t) &= \left(\frac{F_{\text{drive}}^0}{m^*} \cos(\phi_{\text{drive}}) + \frac{F_{\text{piezo}}^0}{m^*} \cos(\phi_{s,1}) \right) \times \cos(\omega t) \\ &\quad - \left(\frac{F_{\text{drive}}^0}{m^*} \sin(\phi_{\text{drive}}) + \frac{F_{\text{piezo}}^0}{m^*} \sin(\phi_{s,1}) \right) \times \sin(\omega t). \end{aligned} \quad (20)$$

As sine and cosine are linearly independent, we can write

$$\frac{\omega\omega_0}{Q} A = \frac{F_{\text{drive}}^0}{m^*} \sin(\phi_{\text{drive}}) + \frac{F_{\text{piezo}}^0}{m^*} \sin(\phi_{s,1}). \quad (21)$$

At a fixed z_0 and constant amplitude A, the left-hand side of Eq. (21) is constant. The two terms on the right-hand side are determined by the amplitudes of the two forces, $F_{\text{drive}}(t)$ and $F_{\text{piezo}}(t)$, that characterize the excitation of the sensor beam. To keep the amplitude A and thus the left-hand side constant, these two terms have to cancel each other out, up to a constant offset given by the setpoint amplitude.

At large enough tunneling currents, where $\langle I_t \rangle$ (and thus F_{piezo}^0) changes so quickly as a function of tip–sample distance that the PI-controller cannot adjust the excitation X'_{drive} (and thus F_{drive}^0) fast enough during a z-sweep measurement, the amplitude A will change accordingly.

The parasitic piezoelectric excitation described by the force $F_{\text{piezo}}(t)$ depends on the presence of a tunneling current. In the limit of the free, mechanically driven cantilever with no tip–sample interaction forces ($\omega = \omega_0$ and $\phi_{\text{drive}} = 90°$) and zero tunneling current [$F_{\text{piezo}}(t) = 0$ N], Eq. (21) simplifies to

$$\frac{F^0_{\text{drive}}}{m^*} = \frac{\omega_0^2}{Q} A|_{\text{free}}, \tag{22}$$

where $A|_{\text{free}}$ denotes the amplitude in the case of a free, driven oscillation, which is directly proportional to the amplitude excitation signal X'_{drive},

$$F^0_{\text{drive}} = \frac{k}{Q}\,\alpha\, X'_{\text{drive}}, \tag{23}$$

where the proportionality factor α is obtained from the experimental data (see Sec. V A).

Meanwhile, the piezoelectric force $F_{\text{piezo}}(t)$ is directly linked to the modulation of $V_s(t)$. We propose an elastic force with

$$F_{\text{piezo}}(t) = (k + k_{\text{ts}}(z_0)) \times q_{\text{pe}}(t), \tag{24}$$

where $q_{\text{pe}}(t)$ is the deflection of the cantilever due to the inverse piezoelectric effect and the AC voltage $V_{s,1} \times \cos(\omega t + \phi_{s,1})$ applied to the STM electrode. For small deflections, the deformation of a piezoelectric crystal is directly proportional to the applied voltage,

$$q_{\text{pe}}(t) = \beta \times V_{s,1}\, \cos(\omega t + \phi_{s,1}) \tag{25}$$

with the proportionality factor β, which can also be determined experimentally (see Sec. V A). As a result, for F^0_{piezo}, one finds

$$F^0_{\text{piezo}} = k\,\frac{\omega^2}{\omega_0^2}\,\beta\, V_{s,1}. \tag{26}$$

To verify if our model agrees with experimental data, we combine the results found so far: solving Eq. (21) for X'_{drive} results in

$$X'_{\text{drive}} = \frac{\omega}{\omega_0}\,\frac{A}{\alpha\,\sin(\phi_{\text{drive}})} + Q\,\frac{\omega^2}{\omega_0^2}\,\frac{\beta\, V_{s,1}\,\sin(\phi_{s,1})}{\alpha\,\sin(\phi_{\text{drive}})}, \tag{27}$$

where $V_{s,1}$ and $\phi_{s,1}$ are found—according to the bias configuration—as described in Secs. IV A 1 and IV A 2, respectively.

Assuming that the first term on the right-hand side in Eq. (27) is independent of $\langle I_t \rangle$ and taking into account that the second term vanished for zero current, the first term can, per definition, be set equal to X_{drive}. Together with Eq. (10), one finds

$$\Delta E^{\text{apparent}}_{\text{ts}} \approx \pi\, k\, A\, \beta \times V_{s,1}\, \sin(\phi_{1,s}), \tag{28}$$

where $\omega/\omega_0 \approx 1$ was used.

V. TESTING THE HARMONIC MODEL

The harmonic model (Sec. IV) is verified by comparing the results from Eq. (27) with the experimental values of the excitation X'_{drive} during z-spectroscopy. More specifically, we compare the values for $\Delta E^{\text{apparent}}_{\text{ts}}/\langle I_t \rangle$, which are obtained from a linear fit of $\Delta E^{\text{apparent}}_{\text{ts}}$ vs $\langle I_t \rangle$: $\Delta E^{\text{apparent}}_{\text{ts}}$ can be calculated using either the measured excitation signal [Eq. (10)] or the theoretical values for $V_{s,1} \times \cos(\omega t + \phi_{s,1})$ [Eq. (27) or Eq. (28)]; the data (phase ϕ_{drive}, angular frequency ω, and amplitude A) needed for calculation [Eq. (27)] stem from the corresponding z-spectroscopy measurements. The decay constant κ can easily be determined: fitting $\langle I_t \rangle$ linearly vs z on a logarithmic scale results in a straight line with slope (-2κ).

The remaining free parameters of Eq. (27) are α and β, which are discussed in the following.

A. Fixing the parameters for the harmonic model

The amplitude of the driving force F^0_{drive} depends on the ratio α of the amplitude $A|_{\text{free}}$ for the case of a free oscillation to the excitation X'_{drive} [see Eq. (23)]. The amplitude response to the mechanical excitation using the piezo-tube simultaneously depends on the overall expansion of the piezo-tube, and α is, therefore, different in the case of a fully withdrawn tip than in the regime, where the z-spectroscopy data were measured. As the excitation X'_{drive} changes according to the apparent dissipation, while conservative forces, such as the tip–sample interaction, only change the frequency shift Δf, leaving amplitude A and excitation X'_{drive} constant, the value of α can also be obtained from the ratio of the measured amplitude A to the excitation X'_{drive} in the case of a finite tip–sample force (finite frequency shift Δf) but vanishing tunneling current $\langle I_t \rangle$. Plotting amplitude A and excitation X'_{drive}, respectively, as a function of $\langle I_t \rangle$ (from the z-spectroscopy data), the values of A and X'_{drive} for $\langle I_t \rangle = 0$ nA can be obtained as the y-offset of a linear fit in both cases; the value of α is, in turn, given by the slope of a linear fit of these values (Fig. 7): here, $\alpha = 192$ nm/V for measurements with bias applied to the tip and $\alpha = 109$ nm/V for measurements with bias applied to the sample.

The amplitude of the piezoelectric force F^0_{piezo}, on the other hand, depends on the value of β, the sensor deflection per voltage drop of 1 V at the STM electrode. It can be obtained from a sweep of the bias voltage applied to the tip.

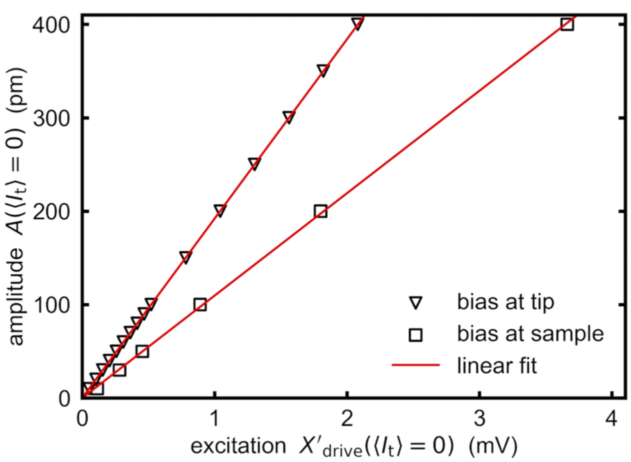

FIG. 7. Determination of α from the data of z-spectroscopy measurement. The values for both amplitude A and excitation X'_{drive} for $\langle I_t \rangle = 0$ nA (which corresponds, to a good approximation, to the case of the free oscillation) are obtained from a linear fit of A and X'_{drive}, respectively, as a function of $\langle I_t \rangle$.

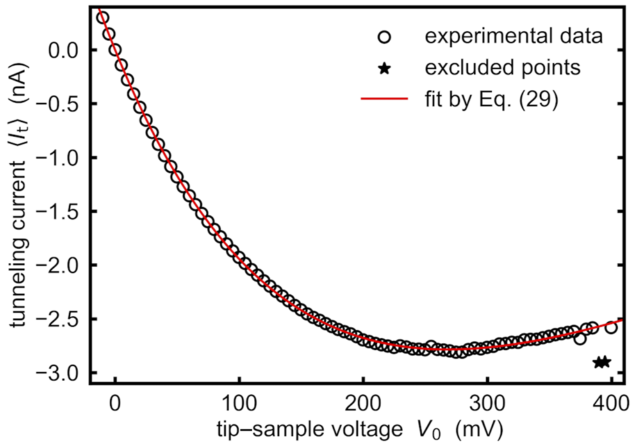

FIG. 8. Tunneling current $\langle I_t \rangle$ vs voltage V_0 applied at the tip. From a fit of experimental data by Eq. (29), the value of β can be obtained. Two data points have been excluded from the fit, which strongly differ from the other data points because of an instability of the tip at high voltages V_0, likely causing a change in the atomic configuration of the tip and thus an abrupt change in the tunneling current $\langle I_t \rangle$.

The tunneling current as a function of the tip–sample distance z is given in Eq. (1), where $I_0 = G_0 V$, in which G_0 is the conductance quantum and V is the potential difference between tip and sample. Since in our simplified model, the sample lies at V_g, which is at ground, $V_s(t)$ equals the voltage between the sensor tip and the sample; in Sec. IV A 1 (with Appendix B 1), it has been shown that the time-average of this potential is given by $V_0 = V_B + R\langle I_t \rangle$.

By the inverse piezoelectric effect, a tip–sample voltage V_0 leads to a change in the tip–sample distance: $z \to z + \beta V_0$. For a given value of z, the tunneling current as a function of the voltage between tip and sample is, therefore,

$$I_t(V_0) = G_0 V_0 \times \exp(-2\kappa(z + \beta V_0)). \tag{29}$$

From a bias voltage sweep in a constant height mode, the experimental values for $I_t(V_0)$ are obtained, which can be fitted by Eq. (29). The decay constant κ is determined from a separate z-spectroscopy measurement: $\kappa = 1.03 \times 10^{10}\ \mathrm{m}^{-1}$. The fit in Fig. 8 results in $\beta = 181$ pm/V.

B. Results

The experimental values for $\Delta E_{ts}^{apparent}/\langle I_t \rangle$ can be obtained from a linear fit of $\Delta E_{ts}^{apparent}$ as a function of $\langle I_t \rangle$. A theoretical result from our model can be obtained by using X'_{drive} as calculated by Eq. (27), instead of experimental data to obtain $\Delta E_{ts}^{apparent}$ [Eq. (10)], as discussed at the beginning of Sec. V; after α and β have been determined, no free parameters are left.

Figure 9 shows a comparison between experiment and theory for the two bias configurations, for multiple oscillation amplitudes A between 10 and 400 pm, as well as for R_B between 0 Ω and 110 kΩ, respectively. In addition, the results for $V_g = 0$ V, obtained from the LTSpice simulation, are plotted. The inset graph focuses on $A \leq 100$ pm, where the assumption $\kappa A \leq 1$ is valid. Here, the behavior of $\Delta E_{ts}^{apparent}/\langle I_t \rangle$ is dominated by the quadratic term $E \propto A^2$ in Eq. (10), while for larger amplitudes, the factor $(X'_{drive}/X_{drive} - 1)$

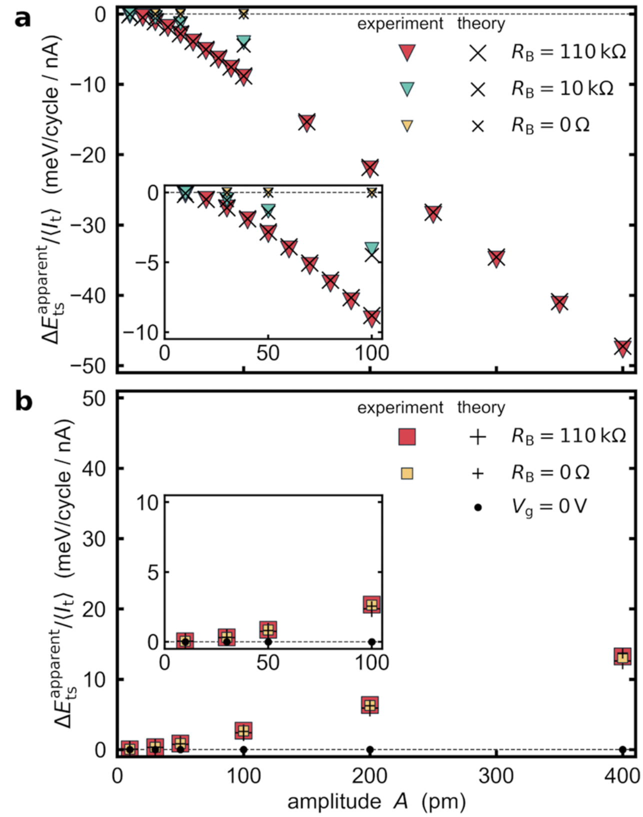

FIG. 9. $\Delta E_{ts}^{apparent}/\langle I_t \rangle$ as a function of amplitude A for different values of R_B. $\Delta E_{ts}^{apparent}$ is obtained from X'_{drive} [experimental values and theoretical calculation by Eq. (27)] using Eq. (10). (a) For bias applied to the tip, the theoretical results for $V_s(t)$ were calculated as discussed in Sec. IV A 1. (b) For bias applied to the sample, $V_s(t)$ was obtained from an LTSpice simulation (see Sec. IV A 2). The results for $V_g = 0$ V were obtained using a corresponding LTSpice simulation without the STM preamplifier. For both bias configurations, the theoretical results start to deviate from experiment at $\kappa A \approx 1$ ($A \approx 100$ pm), where the harmonic approximation is no longer valid.

increases more significantly such that the overall behavior becomes almost linear. Since the results, for given A and R_B, are independent of the ramping direction and the magnitude of the bias $|V_B|$, it is valid to consider the average for both ramping directions and all bias voltages. As discussed in Sec. III B, for bias applied to the tip (sample), $\Delta E_{ts}^{apparent}$ and $\langle I_t \rangle$ have an opposite (the same) sign; $\Delta E_{ts}^{apparent}/\langle I_t \rangle$ is always negative (positive).

1. Bias at tip

From the experimental data with bias applied at the tip, one finds that $\Delta E_{ts}^{apparent}/\langle I_t \rangle$ is reduced to around 45% for $R_B = 10$ kΩ and to less than 1% for $R_B = 0$ Ω (no external resistor), respectively, compared to the values observed with $R_B = 110$ kΩ [Fig. 9(a); for exemplary values, see Appendix A 2 with Table II]; cross coupling becomes negligible as R_B goes to zero.

In general, a very good agreement is found between the theoretical and experimental values. For $A = 10$ pm or $R_B = 0$ Ω,

TABLE II. Values for the apparent dissipated energy per oscillation cycle and tunneling current $\Delta E_{\mathrm{ts}}^{\mathrm{apparent}} / \langle I_{\mathrm{t}} \rangle$ obtained from measurements with up to three different resistors R_{B} in the bias line for an amplitude $A = 50$ pm (see the fits in Fig. 12).

	$\Delta E_{\mathrm{ts}}^{\mathrm{apparent}}/\langle I_{\mathrm{t}}\rangle$ (meV/cycle/nA)	
Resistance R_{B} (kΩ)	Bias at tip	Bias at sample
110	−2.95	0.86
10	−1.33	...
0	−0.01	0.85

$\Delta E_{\mathrm{ts}}^{\mathrm{apparent}}/\langle I_{\mathrm{t}}\rangle$ is close to zero such that the theoretical results lie within the noise level of the experiment. The largest relative error for points with $A > 10$ pm and $R_{\mathrm{B}} > 0\ \Omega$ is 9% for $A = 100$ pm and $R_{\mathrm{B}} = 10$ kΩ; around $\kappa A \approx 1$ ($A \approx 100$ pm), the harmonic approximation of our model is no longer valid (see also Appendix B) such that the values deviate from experiment. Nevertheless, for $R_{\mathrm{B}} = 110$ kΩ, the largest relative error for $A \geq 100$ pm is only 2%, and the average error for $A > 10$ pm, including values for $R_{\mathrm{B}} = 10$ kΩ, is only 6%.

2. Bias at sample

A comparison of experimental data for $\Delta E_{\mathrm{ts}}^{\mathrm{apparent}}/\langle I_{\mathrm{t}}\rangle$ with the theoretical values for $V_{\mathrm{g}} = 0$ V gives a reduction in the apparent dissipation of practically 100% from removing the STM preamplifier [Fig. 9(b); see also Appendix A 2].

Generally, theoretical results ($V_{\mathrm{g}} \neq 0$ V) agree well with experimental results. For $A = 10$ pm, the values again lie below the noise level of experiment. For larger A, the average error is 6% with the maximal relative error of 12% for $R_{\mathrm{B}} = 110$ kΩ and $A = 50$ pm.

3. Summary

In summary, it has been found that depending on the tunneling current, the apparent dissipation is distorted by an additional crosstalk term. The presented model quantifies this dependence and agrees with experimental data within an error margin of 6%, on average. If bias is applied to the tip (sample), the crosstalk term vanishes when the RC element (virtual ground fluctuation) is eliminated, thus significantly improving quantitative dissipation measurement; this was verified by reducing the resistance (grounding the former inverting amplifier input), resulting in negligible $\Delta E_{\mathrm{diss}}^{\mathrm{apparent}}/\langle I_{\mathrm{t}}\rangle$. Possibilities to minimize cross coupling are discussed in detail in Sec. V C. Typical dissipation measurements apply $0V$ bias to mitigate cross coupling; elimination of cross coupling paves the way for simultaneous tunneling current and dissipation measurements. Even with zero bias, noise allows a small current to flow for a very small tip–sample separation; our analysis allows us to account for the contribution of apparent dissipation.

Having reliably quantified the apparent dissipation, the results can easily be transferred to 2D-imaging as well. By comparison with the tunneling current channel and using the values illustrated in Fig. 9, it is possible to separate the crosstalk contribution from the apparent dissipation signal.

Figure 10 shows a comparison of experimental apparent dissipation and theoretically determined apparent dissipation due to cross coupling. The results show excellent agreement.

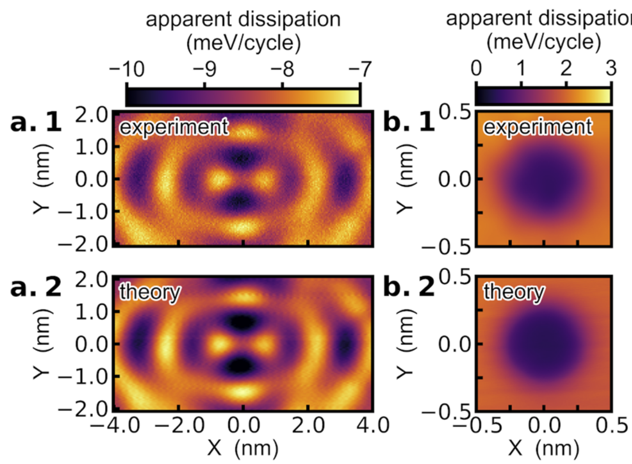

FIG. 10. Experimental and calculated apparent dissipation data. (a) Standing wave pattern inside an elliptical quantum corral[49,50] on Cu(111). Tip bias $V_{\mathrm{B}} = -1.0$ mV. (b) CO molecule on Cu(111). Sample bias $V_{\mathrm{B}} = -1.0$ mV. (a1) and (b1) Experimental data. No real dissipation is expected from (a1) the standing wave pattern itself or (b1) the CO molecule at a large distance from the sample; the signal in the excitation channel is purely apparent dissipation due to cross coupling. A Gaussian filter was applied in (b1) since the signal is small such that noise is significant. (a2) and (b2) Theoretical result calculated from the measured current using the theoretical value of $\Delta E_{\mathrm{ts}}^{\mathrm{apparent}}/\langle I_{\mathrm{t}}\rangle$ for $R_{\mathrm{B}} = 110$ kΩ and $A = 50$ pm in Figs. 9(a) and 9(b), respectively. The theory reproduces the experimental data exceedingly well.

C. Solutions to minimize the cross coupling

The origin of the cross coupling discussed here is a tiny fluctuation on the order of μV of the voltage on the sensor electrode that carries the tunneling current with respect to the other sensor electrodes. According to Eq. (25), a voltage fluctuation of 1 μV shakes the qPlus sensor with an amplitude of 0.18 fm, which, at resonance, with its Q enhancement leads to an amplitude of 36 pm for $Q = 200\,000$. However, this current induced excitation is intrinsically not at the right phase to induce additional excitation or damping. A slight phase shift between this voltage and the tunneling current is needed to drive crosstalk, but this slight phase shift is easily occurring due to parasitic capacities and unavoidable electrical resistances of the leads connecting the bias source with the sensor. Nevertheless, several solutions to prevent crosstalk are possible.

One solution is to provide a separate wire to the tip as already proposed by Heyde *et al.* in 2006[23] and also used in Ref. 26. However, a drawback of this method is that the external wire often lowers the Q-value of the sensor and can even induce side resonances and coupled modes between the sensor and wire oscillations. Furthermore, as discussed in Ref. 24, the oscillating tip and the modulation of the potential at the tip act as an electric dipole, emitting electromagnetic waves that might couple to the excitation of the qPlus sensor via the inverse piezoelectric effect.

Changing the layout of the electrodes on the quartz cantilever itself to effectively shield the STM electrode in a university laboratory is highly non-trivial. Metallized quartz-substrates that form the basis for the qPlus sensor are manufactured by companies that rely on decades of experience and have state-of-the-art technology for etching and metallizing quartz. The minimal width of the electrodes is limited to ~20 μm. If the width could be reduced to 1 μm and the STM electrode was guarded with close ground electrodes, effective shielding would be possible.

One other solution is to intentionally reduce Q and to tolerate the corresponding increase in noise, for instance, in IETS (inelastic electron tunneling spectroscopy) measurements with a high tunneling current under static conditions.[31]

Schwenk *et al.* introduced a rather clean solution in Fig. 9 of Ref. 51, where the potential of the AFM amplifier is lifted to the bias voltage such that a μV fluctuation of the bias voltage does not cause a differential voltage between sensor electrodes.

Another solution would be to modulate the bias voltage signal at the sensor using the same signal phase-shifted by 180° in order to completely cancel the oscillation of the potential at the STM electrode (negative feedback): inductors, such as coils, could be used in order to shift the phase intentionally. However, this solution requires tuning and is complex.

In theory, removing the resistance R would be the easiest solution to get rid of the RC low-pass in the bias line; in practice, however, a finite resistance of the wiring will always remain, in particular in low temperature microscopes where a low thermal (and thus low electrical) conductivity of the wires is needed to reduce helium consumption. As we have seen in Sec. V B, the dissipated energy decreases drastically when removing R_B: the apparent dissipation is negligibly small compared to the case with $R_B = 110$ kΩ. The big disadvantage of this approach is that an alternative kind of noise filter for the bias voltage signal is required since removing R_B also eliminates the RC low-pass filter element in the circuit. One solution to this is adding a buffer amplifier after the RC filter to provide a low impedance source for the bias voltage that is not significantly modulated by the load of typical tunneling currents.

The virtual ground problem can be tackled by adjusting the loop gain of the current amplifier, thereby reducing the effective phase shift of the feedback loop and modulation of V_g. Whether this solution is feasible or not depends on the amplifier used in the setup and also needs to be evaluated by taking into consideration the increase in noise.

By grounding the tip (real ground), the apparent dissipation could be eliminated completely if the ground connections were ideal. In this case, a biased STM preamplifier would have to be used.

VI. SUMMARY

The origin of cross coupling between tunneling current and excitation in a home-built, combined scanning tunneling and atomic force microscope setup has been identified. In dynamic AFM operation modes, such as frequency modulation AFM, where the tip oscillates, the tunneling current flowing through the tip electrode at the sensor will also oscillate as a function of time. If the impedance of the bias voltage supply is not very small, e.g., when using a passive RC low-pass filter without a buffer, or if current amplifier non-idealities are significant, e.g., due to a large input impedance, the oscillating current will cause an oscillation in the voltage at the tip, leading to a cross coupling between excitation and tunneling current. In this study, the origin of such a cross coupling was investigated: the presented quantitative analysis is based on the inverse piezoelectric effect and accounts for the harmonic modulation of the potential at the tip electrode. In our setup, this voltage oscillation is caused by an RC low-pass filter in the experimental setup consisting of a resistance R in the cable that connects the bias output to the sensor and the capacitance C between the STM-electrode of our qPlus sensor and ground, or by the non-ideal behavior of the current amplifier with a high input impedance; in both cases, the oscillating potential on the STM-electrode is shifted out of phase with the sensor oscillation. The measured apparent dissipation signal is linked to a piezoelectric force, which is proportional to the oscillating component of that potential. We have verified the validity of our theoretical model by comparing it with the experimental data. Theoretical and experimental data from z-spectroscopy measurements agree with an error margin of around 12% and an average error that is only half of that, which is quite good, considering the tiny voltage modulations on the μV range.

ACKNOWLEDGMENTS

The authors thank Ferdinand Huber and Julian Berwanger for providing initial current vs damping data and Jay Weymouth for discussions. M.S. further thanks Raphael Lehner, who helped him with some calculations. The authors also acknowledge the Deutsche Forschungsgemeinschaft for funding under Grant Nos. CRCs 689 and 1277.

AUTHOR DECLARATIONS

Conflict of Interest

Yes, F.J.G. holds German patent DE 10 2010052037, US patent 8393009 and Chinese patent No. ZL201110373640.3 about the force sensor that was used in the experiments. The remaining authors have no conflicts to disclose.

Author Contributions

Michael Schelchshorn: Investigation (equal); Methodology (equal); Visualization (equal); Writing – original draft (equal); Writing – review & editing (equal). **Fabian Stilp**: Supervision (equal); Writing – review & editing (supporting). **Marco Weiss**: Supervision (equal); Writing – review & editing (supporting). **Franz J. Giessibl**: Conceptualization (equal); Supervision (equal); Writing – original draft (equal); Writing – review & editing (equal).

DATA AVAILABILITY

The data that support the findings of this study are available from the corresponding authors upon reasonable request.

APPENDIX A: SUPPLEMENTARY EXPERIMENTAL DATA

1. Testing the virtual ground of the STM preamplifier

In Sec. III A, it is stated that if bias is applied at the tip, the apparent dissipation $\Delta E_{ts}^{apparent}$ with the STM preamplifier disconnected is equal to $\Delta E_{ts}^{apparent}$ in the case with the amplifier connected such that V_g can be assumed to be at ground. For the two cases (with and without the STM preamplifier) as well as the two bias configurations, Fig. 11 shows a comparison of the apparent dissipation

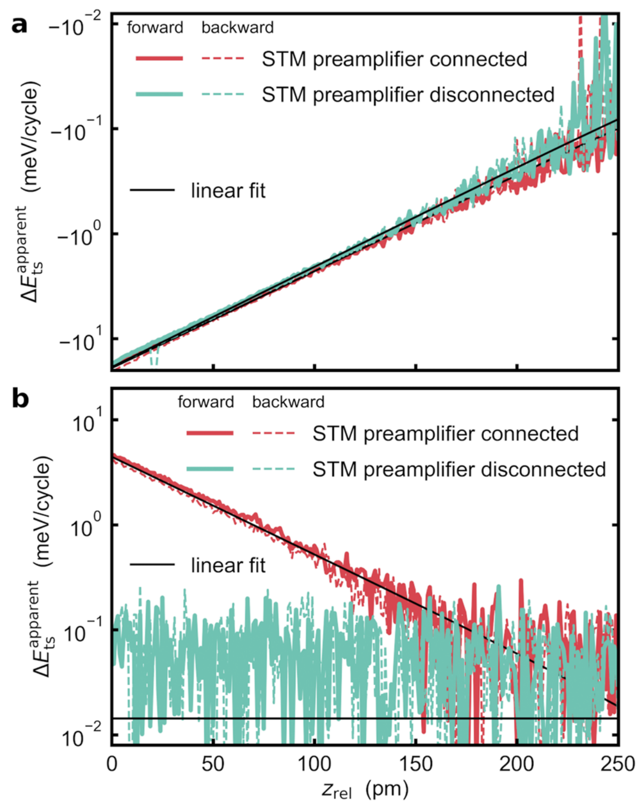

FIG. 11. Comparison of $\Delta E_{ts}^{apparent}$ for measurements with the STM preamplifier connected (as depicted in Fig. 3) as well as the amplifier disconnected; in the latter case (turquoise curves), one has the (a) sample grounded and (b) tip grounded. The relative tip height z_{rel} was chosen as the x axis since the tunneling current cannot be measured with the preamplifier disconnected. The discrepancy in the backward (dashed) lines can be attributed to piezo-creep. The step in the backward sweep in (a) is due to tip instability.

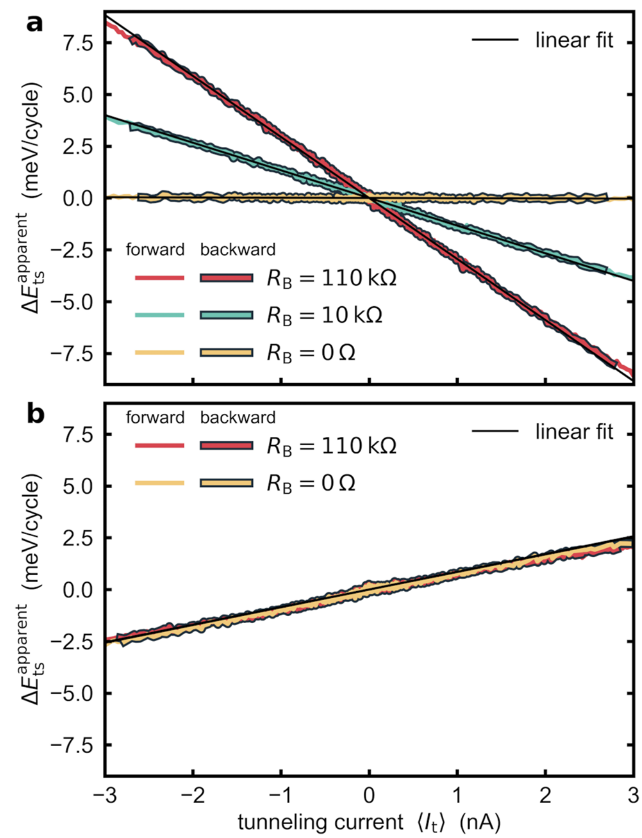

FIG. 12. $\Delta E_{ts}^{apparent}$ for different values of R_B, for forward and backward ramping directions of the z-spectroscopy, respectively, for $A = 50$ pm and $V_B = \pm 1.0$ mV. (a) Bias applied at the tip. (b) Bias applied at the sample. The slopes of the curves as obtained from a linear fit correspond to the values in Table II. The graphs also make it clear that $\Delta E_{ts}^{apparent}/\langle I_t \rangle$ is, in general, independent of the ramping direction during measurement.

$\Delta E_{ts}^{apparent}$ as a function of the relative tip height z_{rel} for forward and backward directions, respectively. With the STM preamplifier disconnected, the tip is approached in AFM feedback using the same frequency shift setpoint at $z_{rel} = 0$ pm as for the measurement with the STM preamplifier connected.

The slopes of linear fits in Fig. 11(a) (bias applied at the tip) agree within an error of 2%, suggesting that $V_g = 0$ V is a reasonable approximation. The tip instability caused a step at around $z_{rel} = 20$ pm in the backward measurements with the STM preamplifier disconnected.

For bias applied to the sample [Fig. 11(b)], the slope of the linear fit decreases by close to 100%, indicating that $\Delta E_{ts}^{apparent}/\langle I_t \rangle$ is equally reduced when grounding the former inverting input of the STM preamplifier.

2. Different R_B, ramping directions, and piezo-creep

In Fig. 12, $\Delta E_{ts}^{apparent}$ is plotted as a function of tunneling current $\langle I_t \rangle$ for forward and backward ramping directions for an amplitude of $A = 50$ pm and different values of R_B. A linear fit of the curves for each of these values for R_B gives the values for $\Delta E_{ts}^{apparent}/\langle I_t \rangle$ listed in Table II.

From the graphs (Fig. 12) is also evident that $\Delta E_{ts}^{apparent}$ is independent of the ramping direction during measurement as stated in Sec. III B. This is valid as long as the ramping speed is chosen slow enough for the PI-controller to be able to effectively control the excitation to keep the oscillation amplitude constant as mentioned in Sec. IV B.

The maximal tunneling currents in the backward ramps are about 10% smaller compared to the forward ramps as during measurement, a drift in the z-position of the tip, for example due to piezo-creep, can occur. When the tip is moved 500 pm away from and again 500 pm toward the sample during the z-spectroscopy measurement, the value of the tunneling current at the end will differ from the value at the beginning of the measurement by 10% if the total distance z has merely changed by 5 pm (i.e., 1%). This effect was minimized by performing a drift-compensation before each measurement, which helps, for example, for a thermal drift, but not for the piezo-creep originating from the z-position movement during the z-spectroscopy experiments.

APPENDIX B: CALCULATION OF SENSOR POTENTIAL FOR BIAS AT TIP AND VALIDITY OF THE HARMONIC MODEL

Here, the sensor potential $V_s(t)$ [Eq. (14)] as used in the harmonic model of Sec. IV is calculated.

Furthermore, we show that the assumption of a harmonic tunneling current $I_t(t)$ is justified by explicitly performing the calculation with the tunneling current given by Eq. (5).

The defining differential equation for the sensor potential $V_s(t)$, Eq. (13), is an inhomogeneous linear differential equation of the form

$$\frac{\mathrm{d}V_s(t)}{\mathrm{d}t} = a(t)\, V_s(t) + b(t), \tag{B1}$$

where a and b are continuous functions of time t given by

$$a(t) = -1/RC \quad \text{and} \quad b(t) = I_t(t)/C + V_B/RC. \tag{B2}$$

The unique solution to the differential equation (B1) with initial condition $V_s(t_0) = c$ ($t_0, c \in \mathbb{R}$) is given by[52]

$$V_s(t) = V_0(t)\left(c + \int_{t_0}^{t} V_0(t')^{-1}\, b(t')\,\mathrm{d}t'\right), \tag{B3}$$

where

$$V_0(t) = \exp\left(\int_{t_0}^{t} a(t')\,\mathrm{d}t'\right) \tag{B4}$$

is the solution to the homogeneous differential equation, i.e., Eq. (B1) with $b(t) = 0$.

If we choose the initial time as $t_0 = 0$, we have

$$V_0(t) = \exp(-t/RC) \quad \text{and} \quad V_0(t)^{-1} = \exp(t/RC). \tag{B5}$$

Putting everything together in Eq. (B3) gives

$$\begin{aligned} V_s(t) &= (V_s(0) - V_B) \times \exp(-t/RC) + V_B \\ &\quad + \exp(-t/RC) \times \int_0^t \exp(t'/RC)\, I_t(t')/C\,\mathrm{d}t', \end{aligned} \tag{B6}$$

where $I_t(t')$ denotes the time-dependent tunneling current as discussed in Sec. II C.

1. Harmonic tunneling current

Before turning to the more rigorous calculation, the current is considered only up to first order in ω,

$$I_t(t) = \langle I_t \rangle + I_{1\omega} \times \cos(\omega t). \tag{B7}$$

Inserting this into Eq. (B6) and using Euler's formula to solve the integral yields

$$\begin{aligned} V_s(t) &= \left[V_s(0) - \left(V_B + R\langle I_t\rangle + \frac{R\, I_{1\omega}}{1 + (\omega RC)^2}\right)\right] \\ &\quad \times \exp(-t/RC) + V_B + R\langle I_t\rangle \times v_s(t), \end{aligned} \tag{B8}$$

where

$$v_s(t) = \frac{R\, I_{1\omega} \cos(\omega t - \arctan(\omega RC))}{\sqrt{1 + (\omega RC)^2}}. \tag{B9}$$

Leaving out the transient terms that decay exponentially with time t, one finds the steady-state solution for $V_s(t)$ as stated in Eq. (14).

2. Inharmonic tunneling current

To show that assuming a harmonic behavior of V_s is valid, the sensor potential can also be calculated by inserting the actual tunneling current,

$$\begin{aligned} I_t(t) &\overset{\text{Eq. (5)}}{=} I_{z_0} \times \exp(-2\kappa A \cos(\omega t)) \\ &\overset{\text{Eq. (7)}}{=} \frac{\langle I_t\rangle}{\mathfrak{I}_0(2\kappa A)} \times \exp(-2\kappa A \cos(\omega t)), \end{aligned} \tag{B10}$$

into Eq. (B6). Using again Euler's formula, the series expansion of the exponential, and

$$\mathfrak{I}_l(2x) = \sum_{n=0}^{\infty} \frac{x^{2n+l}}{n!(n+l)!} \qquad (x \geq 0), \tag{B11}$$

the result can be rewritten as

$$V_s(t) = (V_s(0) - V_B - R\langle I_t\rangle) \times \exp(-t/RC) + V_B + R\langle I_t\rangle + u_s(t), \tag{B12}$$

where

$$\begin{aligned} u_s(t) &= \frac{2R\langle I_t\rangle}{\mathfrak{I}_0(2\kappa A)} \sum_{\substack{n=0\\m=1\\n<m}}^{\infty} \frac{(-\kappa A)^{n+m}}{n!\,m! \times [1 + (\omega RC(m-n))^2]} \\ &\quad \times \{\cos(\omega t(m-n)) - \exp(-t/RC) + \omega RC(m-n) \\ &\quad \times \sin(\omega t(m-n))\}. \end{aligned} \tag{B13}$$

Neglecting all terms with an exponentially decaying factor, one has

$$V_s(t) = V_B + R\langle I_t\rangle + u_s(t) \tag{B14}$$

and

$$\begin{aligned} u_s(t) &= \frac{2R\langle I_t\rangle}{\mathfrak{I}_0(2\kappa A)} \sum_{\substack{n=0\\m=1\\n<m}}^{\infty} \frac{(-\kappa A)^{n+m}}{n!\,m!} \\ &\quad \times \frac{\cos[\omega t(m-n) - \arctan(\omega RC(m-n))]}{\sqrt{1 + (\omega RC(m-n))^2}}. \end{aligned} \tag{B15}$$

The terms of first order in ω correspond to the terms of the sum, where $m = n + 1$; the second order terms correspond to $m = n + 2$; and so on; hence, with Eq. (B11), we find

$$u_s(t) = v_s(t) + \sum_{l=2}^{\infty} \frac{R\, I_{l\omega} \cos(l\omega t - \arctan(l\omega RC))}{\sqrt{1 + (l\omega RC)^2}}, \tag{B16}$$

where

$$I_{l\omega} = (-1)^l \times 2\langle I_t\rangle \frac{\mathfrak{I}_l(2\kappa A)}{\mathfrak{I}_0(2\kappa A)}, \qquad l = 1, 2, 3, \ldots, \tag{B17}$$

are the Fourier components of the tunneling current of first and higher orders (see Sec. II C).

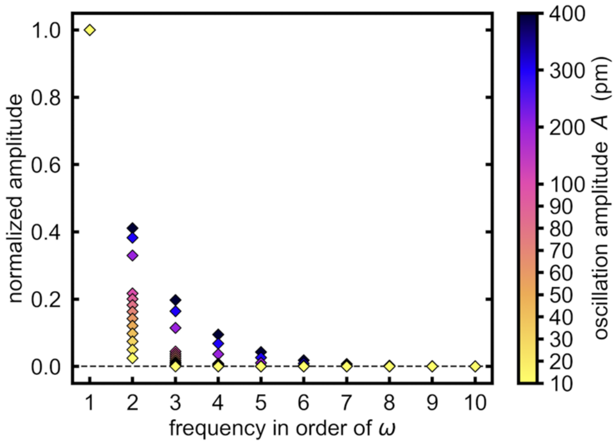

FIG. 13. Amplitude of the first and higher order terms in $u_s(t)$ sorted by order in ω and normalized to the amplitude of the first order term, for different oscillation amplitudes A. The parameters used for the plot are $\kappa = 1 \times 10^{10}$ m^{-1}, $\omega/(2\pi) = 20.4$ kHz, $R = 110.1$ kΩ, and $C = 780$ pF. For $\kappa A \geq 1$ ($A \geq 100$ pm), the second order term is larger than one fifth of the first order term; here, the harmonic approximation breaks down.

The second and higher order terms in $u_s(t)$ are small compared to $v_s(t)$ if $\kappa A < 1$, since the sum in Eq. (B15) converges quickly.

Figure 13 shows the amplitudes of the terms in $u_s(t)$ up to the tenth order in ω for different oscillation amplitudes A between 10 and 400 pm, normalized to the amplitude of the first order term $v_s(t)$. For $A < 100$ pm, already the fifth order term has a negligible amplitude; for $A = 400$ pm, only the tenth and higher order terms are negligibly small. Adopting a harmonic oscillation of the tunneling current $I_t(t)$ for the calculation of the sensor potential $V_s(t)$ is, therefore, justified; the equation of motion of the harmonic oscillator, including the assumption of a harmonic (piezoelectric) dissipative force $F_{\mathrm{piezo}}(t)$, is an appropriate way of describing the dynamic motion of the tip affected by a parasitic dissipation if $\kappa A < 1$. For larger tip amplitudes A, the harmonic approximation breaks down; here, the second order term is already larger than one fifth of the amplitude of $v_s(t)$.

REFERENCES

[1] G. Binnig, H. Rohrer, C. Gerber, and E. Weibel, Appl. Phys. Lett. **40**, 178 (1982).
[2] G. Binnig, H. Rohrer, C. Gerber, and E. Weibel, Phys. Rev. Lett. **49**, 57 (1982).
[3] G. Binnig, H. Rohrer, C. Gerber, and E. Weibel, Phys. Rev. Lett. **50**, 120 (1983).
[4] G. Binnig, C. F. Quate, and C. Gerber, Phys. Rev. Lett. **56**, 930 (1986).
[5] G. Binnig, U.S. patent US4724318A (February 9, 1986).
[6] C. J. Chen, *Introduction to Scanning Tunneling Microscopy*, 3rd ed. (Oxford University Press, 2021).
[7] F. J. Giessibl and G. Binnig, Ultramicroscopy **42–44**, 281 (1992).
[8] *Noncontact Atomic Force Microscopy*, edited by S. Morita, R. Wiesendanger, and E. Meyer (Springer-Verlag, Berlin, Heidelberg, 2002).
[9] *Noncontact Atomic Force Microscopy*, edited by S. Morita, F. J. Giessibl, and R. Wiesendanger (Springer-Verlag, Berlin Heidelberg, 2009), Vol. 2.
[10] *Noncontact Atomic Force Microscopy*, edited by S. Morita, F. J. Giessibl, E. Meyer, and R. Wiesendanger (Springer International Publishing, Switzerland, 2015), Vol. 3.
[11] R. García and R. Pérez, Surf. Sci. Rep. **47**, 197 (2002).
[12] F. J. Giessibl, Rev. Mod. Phys. **75**, 949 (2003).
[13] F. J. Giessibl, Rev. Sci. Instrum. **90**, 011101 (2019).
[14] G. Binnig, Ultramicroscopy **42–44**, 7 (1992).
[15] F. Ohnesorge and G. Binnig, Science **260**, 1451 (1993).
[16] F. J. Giessibl, Science **267**, 68 (1995).
[17] T. R. Albrecht, P. Grütter, D. Horne, and D. Rugar, J. Appl. Phys. **69**, 668 (1991).
[18] P. Günther, U. C. Fischer, and K. Dransfeld, Appl. Phys. B **48**, 89 (1989).
[19] K. Karrai and R. D. Grober, Appl. Phys. Lett. **66**, 1842 (1995).
[20] J. Rychen, T. Ihn, P. Studerus, A. Herrmann, and K. Ensslin, Rev. Sci. Instrum. **70**, 2765 (1999).
[21] F. J. Giessibl, Appl. Phys. Lett. **73**, 3956 (1998).
[22] F. J. Giessibl, Appl. Phys. Lett. **76**, 1470 (2000).
[23] M. Heyde, G. H. Simon, H.-P. Rust, and H.-J. Freund, Appl. Phys. Lett. **89**, 263107 (2006).
[24] L. Nony, F. Bocquet, F. Para, and C. Loppacher, Phys. Rev. B **94**, 115421 (2016).
[25] A. J. Weymouth, T. Wutscher, J. Welker, T. Hofmann, and F. J. Giessibl, Phys. Rev. Lett. **106**, 226801 (2011).
[26] Z. Majzik, M. Setvín, A. Bettac, A. Feltz, V. Cháb, and P. Jelínek, Beilstein J. Nanotechnol. **3**, 249 (2012).
[27] B. J. Albers, M. Liebmann, T. C. Schwendemann, M. Z. Baykara, M. Heyde, M. Salmeron, E. I. Altman, and U. D. Schwarz, Rev. Sci. Instrum. **79**, 033704 (2008).
[28] F. J. Giessibl and M. Tortonese, Appl. Phys. Lett. **70**, 2529 (1997).
[29] F. J. Giessibl, Phys. Rev. B **56**, 16010 (1997).
[30] W. Denk and D. W. Pohl, Appl. Phys. Lett. **59**, 2171 (1991).
[31] N. Okabayashi, T. Frederiksen, A. Liebig, and F. J. Giessibl, Phys. Rev. B **108**, 165401 (2023).
[32] A. J. Weymouth, O. Gretz, E. Riegel, and F. J. Giessibl, Jpn. J. Appl. Phys. **61**, SL0801 (2022).
[33] L. Prandtl, ZAMM **8**, 85 (1928).
[34] G. A. Tomlinson, London, Edinburgh Dublin Philos. Mag. J. Sci. **7**, 905 (1929).
[35] J. P. Cleveland, B. Anczykowski, A. E. Schmid, and V. B. Elings, Appl. Phys. Lett. **72**, 2613 (1998).
[36] N. Sasaki and M. Tsukada, Jpn. J. Appl. Phys. **39**, L1334 (2000).
[37] F. Huber, S. Matencio, A. J. Weymouth, C. Ocal, E. Barrena, and F. J. Giessibl, Phys. Rev. Lett. **115**, 066101 (2015).
[38] F. Huber, "Atomar aufgelöste Messung der lokalen Austrittsarbeit mit kombinierter Rasterkraft- und Rastertunnelmikroskopie," M.Sc. thesis, University of Regensburg, Germany, 2013.
[39] M. Herz, C. Schiller, F. J. Giessibl, and J. Mannhart, Appl. Phys. Lett. **86**, 153101 (2005).
[40] M. Schneiderbauer, "Aufbau eines Tieftemperatur-Ultrahochvakuum-Rasterkraftmikroskops und Messung elektrischer Multipolkräfte im Piconewton-Bereich," Ph.D. dissertation, University of Regensburg, Germany, 2014.
[41] M. Emmrich, "Subatomare Auflösung auf Adatomen und kraftfeldabhängige laterale Manipulation mit einem eigenentwickelten Tieftemperatur-Rasterkraftmikroskop," Ph.D. dissertation, University of Regensburg, Germany, 2015.
[42] Analog Devices Inc., One Technology Way, Norwood, MA, www.analog.com.
[43] P. Horowitz and W. Hill, *The Art of Electronics*, 3rd ed. (Cambridge University Press, 2015).
[44] P. Horowitz and W. Hill, *The Art of Electronics: The X Chapters* (Cambridge University Press, 2020).
[45] V. Junk, "*Characterizing the virtual ground and its link to dissipation effects in simultaneous STM/AFM measurements*," B.Sc. thesis, University of Regensburg, Germany, 2015.
[46] C. Lotze, M. Corso, K. J. Franke, F. von Oppen, and J. I. Pascual, Science **338**, 779 (2012).
[47] Analog Devices Inc., version XVII, www.analog.com/en/design-center/design-tools-and-calculators/ltspice-simulator.html, 2023.

[48]Analog Devices Inc., developed by VW ADSJ, revised version 2.0, www.analog.com/en/products/ad8616.html#product-tools, 2012.
[49]H. C. Manoharan, C. P. Lutz, and D. M. Eigler, Nature **403**, 512 (2000).
[50]F. Stilp, A. Bereczuk, J. Berwanger, N. Mundigl, K. Richter, and F. J. Giessibl, Science **372**, 1196 (2021).
[51]J. Schwenk, S. Kim, J. Berwanger, F. Ghahari, D. Walkup, M. R. Slot, S. T. Le, W. G. Cullen, S. R. Blankenship, S. Vranjkovic, H. J. Hug, Y. Kuk, F. J. Giessibl, and J. A. Stroscio, Rev. Sci. Instrum. **91**, 071101 (2020).
[52]O. Forster, *Analysis 2* (Springer Fachmedien Wiesbaden, 2017), pp. 157–159.